Journal Pre-proof

Ultrastrong and ductile $(CoCrNi)_{94}Ti_3Al_3$ medium-entropy alloys via introducing multi-sacle heterogeneous structures

Jianying Wang , Jianpeng Zou , Hailin Yang , Xixi Dong ,
Peng Cao , Xiaozhou Liao , Zhilin Liu , Shouxun Ji

Please cite this article as: Jianying Wang , Jianpeng Zou , Hailin Yang , Xixi Dong , Peng Cao , Xiaozhou Liao , Zhilin Liu , Shouxun Ji , Ultrastrong and ductile $(CoCrNi)_{94}Ti_3Al_3$ medium-entropy alloys via introducing multi-sacle heterogeneous structures, *Journal of Materials Science & Technology* (2022), doi: https://doi.org/10.1016/j.jmst.2022.06.048

Highlights

- A three-level heterogeneous structure was introduced in CoCrNi alloy.
- $(CoCrNi)_{94}Ti_3Al_3$ delivers ultimate tensile strength of 1.6 GPa and strain of 13.1%.
- Heterogeneous matrix, γ' precipitate and defects led to high strength and ductility.

Ultrastrong and ductile $(CoCrNi)_{94}Ti_3Al_3$ medium-entropy alloys via introducing multi-sacle heterogeneous structures

Jianying Wang [a], Jianpeng Zou [a], Hailin Yang [a, *], Xixi Dong [b], Peng Cao [c], Xiaozhou Liao [d], Zhilin Liu [e, *], Shouxun Ji [b]

[a] State Key Laboratory of Powder Metallurgy, Central South University, Changsha 410083, China

[b] Brunel Centre for Advanced Solidification Technology (BCAST), Brunel University London, Uxbridge, Middlesex, UB8 3PH, United Kingdom

[c] Department of Chemical and Materials Engineering, The University of Auckland, 1142, New Zealand

[d] School of Aerospace, Mechanical & Mechatronic Engineering, The University of Sydney, Sydney, NSW 2006, Australia

[e] Light Alloy Research Institute, College of Mechanical and Electrical Engineering, Central South University, Changsha 410083, China

* Corresponding authors.

E-mail addresses: y-hailin@csu.edu.cn (H.L. Yang); zhilin.liu@csu.edu.cn (Z.L. Liu).

Abstract

The coarsening-grained single-phase face-centered cubic (fcc) medium-entropy alloys (MEAs) normally exhibit insufficient strength for some engineering applications. Here, superior mechanical properties with ultimate tensile strength of 1.6 GPa and fracture strain of 13.1% at ambient temperature have been achieved in a $(CoCrNi)_{94}Ti_3Al_3$ MEA by carefully architecting the multi-scale heterogeneous structures. Electron microscopy characterization indicates that the superior mechanical properties mainly originated from the favorable heterogeneous fcc matrix (1–40 μm) and coherent spherical γ' precipitate (10–100 nm), together with a high number density of crystalline defects (2–10 nm), including dislocations, small stacking faults, Lomer–Cottrell locks, and ultrafine deformation twins.

Keywords: Medium-entropy alloys; Mechanical properties; Heterogeneous structure; γ' nanoprecipitates; Crystalline defects

1. Introduction

High-entropy alloys (HEAs) and medium-entropy alloys (MEAs) have introduced a new alloying strategy and expanded the alloy design greatly by a combination of multiple principal elements in equiatomic or nearly equiatomic concentrations [1, 2]. Among the MEAs and HEAs, the CoCrNi alloy with low stacking fault energy (SFE) tends to easily generate various crystalline defects, including stacking faults (SFs), Lomer–Cottrell locks (LC locks), and twins. These crystalline defects can enhance ductility by providing pathways for the gliding or cross-slipping dislocations, which may deliver excellent ductility and fracture toughness at room temperature and/or cryogenic scenarios [3–5]. Unfortunately, the low strength in as-cast CoCrNi alloy (yield strength normally lower than 400 MPa) becomes insufficient for many engineering applications. Some essential technical developments have been made towards enhancing the mechanical properties [4, 6–9].

Various approaches have been exerted to strengthen the CoCrNi alloys, including boron- and nitrogen- doping [10, 11], coherent precipitates, brittle intermetallics [12–14] as well as grain refinement [15, 16]. Among these approaches, grain refinement via severe plastic deformation (SPD), such as high-pressure torsion (HPT), is usually only appropriate for fabricating small samples, which cannot satisfy the requirements for a wide range of engineering applications [17]. However, grain refinement through thermo-mechanical processing and subsequent full recrystallization enable to produce large samples with relatively homogenous microstructures, further improving the yield strength. Unluckily, this approach might reduce hardenability dramatically, resulting in a limited enhancement in ultimate strength but a significant loss in ductility [18].

4

Interestingly, tailoring microstructures at multi-scales from micrometers even down to nanometers is considered as an effective approach to realize good strength–ductility synergy by enhancing the hetero-deformation induced (HDI) strain hardening ability [12, 13, 19–31]. The representative structures, reported in the Cu alloys, Al alloys, 304/304L stainless steels, MEAs/HEAs, and others, include gradient grain structures [19–24], heterogeneous lamellar structures [25, 26], laminate structures [27, 28], precipitates [12, 13], and nanoscale crystalline defects (dislocation / dislocation cells [29], nanotwins [30, 31]). Recently, it was also found that architecting heterogeneous grain structures can remarkably improve tensile strength and ductility of CoCrNi alloys [21–24]. Nevertheless, the excellent mechanical performances of the CoCrNi-based alloys significantly depend on complex thermal-mechanical processing, including hot rolling, room/cryogenic-temperature rolling, and subsequent two/three-step annealing [22, 23]. For instance, the heterogeneous grain structures containing nanocrystalline grains, ultrafine grains, and micro-grains in the pure CoCrNi alloy can deliver a reasonable trade-off between strength and ductility after the complex thermal-mechanical processing with homogenization, hot-forging, cold rolling, annealing, and water quenching [22].

It is reported that a small amount of Al and Ti, strong gamma-prime phase (γ') formers, can introduce coherent precipitates and deliver excellent strength-ductility synergy [12, 23, 32, 33]. The precipitation strengthening effect of γ'-hardened CoCrNi alloy is generally regulated through tailoring the size and distribution of γ' precipitates, and fine-tuning the content of Ti and Al elements, such as $(CoCrNi)_{94}Ti_3Al_3$ [12, 23], $Co_{34.5}Cr_{32}Ni_{27.5}Al_3Ti_3$ [32], and $(CoCrNi)_{96}Ti_2Al_2$ [33]. However, tailoring the size and distribution of γ' precipitates requires

complex thermal-mechanical processing [12, 23, 32, 33]. Therefore, this work explores a single-step heat treatment to obtain high strength and ductility in a $(CoCrNi)_{94}Ti_3Al_3$ alloy by introducing nano-sized heterogeneous γ' precipitates and different crystalline defects, including dislocations, SFs, LC Locks, and deformation twins in the heterogeneous refined fcc matrix. Our ultimate aim is to obtain good combinations of strength and ductility in soft fcc MEAs/HEAs by fabricating the multi-scale heterogeneous structures. This strategy may also provide some insights into developing high-strength MEAs/HEAs with excellent ductility.

2. Experimental Section

2.1. Materials fabrication

MEA ingots with the chemical composition of $CoCrNi)_{94}Ti_3Al_3$ (at.%) were prepared in a vacuum magnetic levitation melting furnace using pure metals (purity > 99.5 wt%). The chemical compositions of the as-cast ingot are determined using inductively coupled plasma atomic emission spectroscopy (ICP-AES), as listed in Table 1. The as-cast ingots with dimensions of 20 mm × 20 mm × 50 mm were homogenized at 1100 °C for 2.5 h in a protective argon atmosphere, followed by furnace cooling. Subsequently, all the cubic samples were rolled by a 70% reduction in thickness at room temperature. Then, annealing treatment was applied at 500 °C (defined as RA-500 treatment) and 700 °C (defined as RA-700 treatment) for 1 h, respectively.

Table 1 The determined chemical compositions of $(CoCrNi)_{94}Ti_3Al_3$ (at.%).

Cr	Ni	Ti	Co	Al
31.63%	32.54%	3.16%	29.79%	2.88%

2.2. Microstructural characterization

Microstructural features of the alloys were analysed using multiple electron microscopes. Scanning electron microscopy (SEM), electron channeling contrast imaging (ECCI), and electron backscattered diffraction (EBSD) analysis were conducted in a FIB Helios NanoLab G3 UC SEM that is equipped with the TSL OIM data analysis software. Before the ECCI and EBSD characterization, the sample surfaces were firstly ground using silicon carbide paper from 400 to 2000 grit, followed by polishing with 3 and 1 μm diamond suspensions. Fine polishing was performed using a 40 nm colloidal silica suspension for more than half an hour to effectively remove the deformation layer that was caused by previous mechanical grinding. The volume fraction and grain size distribution of precipitates were measured using Image J software. To explore different deformation mechanisms, we further characterized the detailed microstructures by transmission electron microscopy (TEM; Tecnai G2 F20). The mechanically polished TEM samples were thinned using a precision ion polishing system (PIPS) at a voltage of 5 kV and an incident angle of 5°.

2.3. Mechanical property testing

Dog-bone-shaped tensile samples with a gauge length of 30 mm and cross-section of 2.2 mm × 1.5 mm were prepared using electrical discharge machining. Uniaxial tensile tests with a fixed strain rate of 1×10^{-3} s^{-1} were performed at room temperature (25 °C) using an MTS Alliance RT30 mechanical testing system. Micro-hardness was measured by a

micro-Vickers hardness tester with a load of 300 g for 10 s (ASTM E 384-08). All the reported data are based on the average value of at least five measurements. To minimize the measurement errors, the measured mechanical properties were obtained based on an average value collected from over six tests.

3. Results and discussion

SEM/TEM images in Fig. 1(a–c) show the microstructures in the $(CoCrNi)_{94}Ti_3Al_3$ alloy after RA-500 and RA-700 treatments. The RA-500 sample consists of a high number density of heterogeneous precipitates with sizes ranging from 10 to 100 nm, as shown in Fig. 1(a). However, the RA-700 sample has much fewer homogenous coarsening precipitates (~ 100 nm), as shown in Fig. 1(b). Correspondingly, the grain size distribution of precipitates is shown in Fig. 1(d, e). The volume fraction and size of the precipitates detected in the RA-500 sample were 42.8% and 31.6 nm, respectively. The volume fraction and size of precipitates detected in the RA-700 sample were 21.2% and 93.3 nm, respectively. The precipitates of the RA-500 sample were further examined in the bright-field (BF) TEM image (Fig. 1(c)). The selected area electron diffraction (SAED) pattern (L1) inserted in Fig. 1(c) confirmed that the interface of fcc/γ' has a good orientation with $[011]_{fcc}//[011]_{\gamma'}$. Qualitative chemical analysis of the γ' precipitates detected in the alloys after RA-500 and RA-700 treatments was further performed using scanning TEM equipped with energy dispersive X-ray spectroscopy (STEM-EDS), as shown in Fig. 1(f_1–g_5). These γ' precipitates were evidently enriched in Ni, Ti, and Al, but depleted in Co and Ni. Only 3 at% Ti and 3 at% Al were able to promote formation of γ' precipitate, which was consistent with previous studies [12,23]. Additionally, the number density of γ' precipitates after RA-500 treatment

8

(Fig. 1(f_1–f_5)) is also higher than those after RA-700 treatment (Fig. 1(g_1–g_5)), while the size

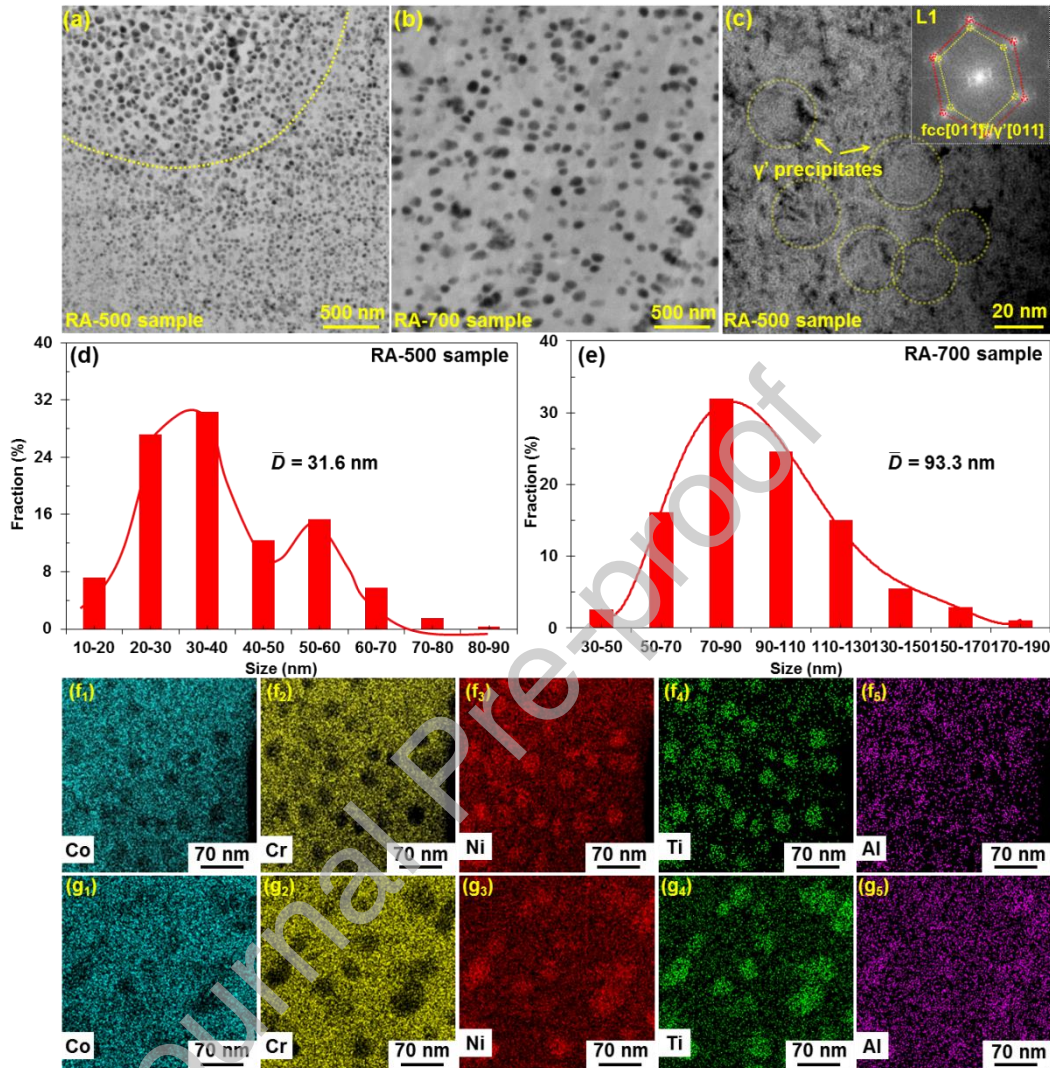exhibits the opposite trend, which agreed well with the SEM results in Fig. 1(a, b).

Fig. 1. (a) SEM image showing the heterogeneous γ' precipitates in the CoCrNi)$_{94}$Ti$_3$Al$_3$ alloy with RA-500

treatment. (b) SEM image showing the homogeneous γ' precipitates in the alloy with RA-700 treatment. (c)

BF-TEM image of the nano-size γ' precipitates and SAED pattern L1, indicating the coherent interface

between fcc matrix and γ' precipitates. (d) and (e) Grain size distribution of the γ' precipitates after RA-500

and RA-700 treatments, respectively. (f_1–f_5) The corresponding STEM-EDS maps of γ' precipitates in the

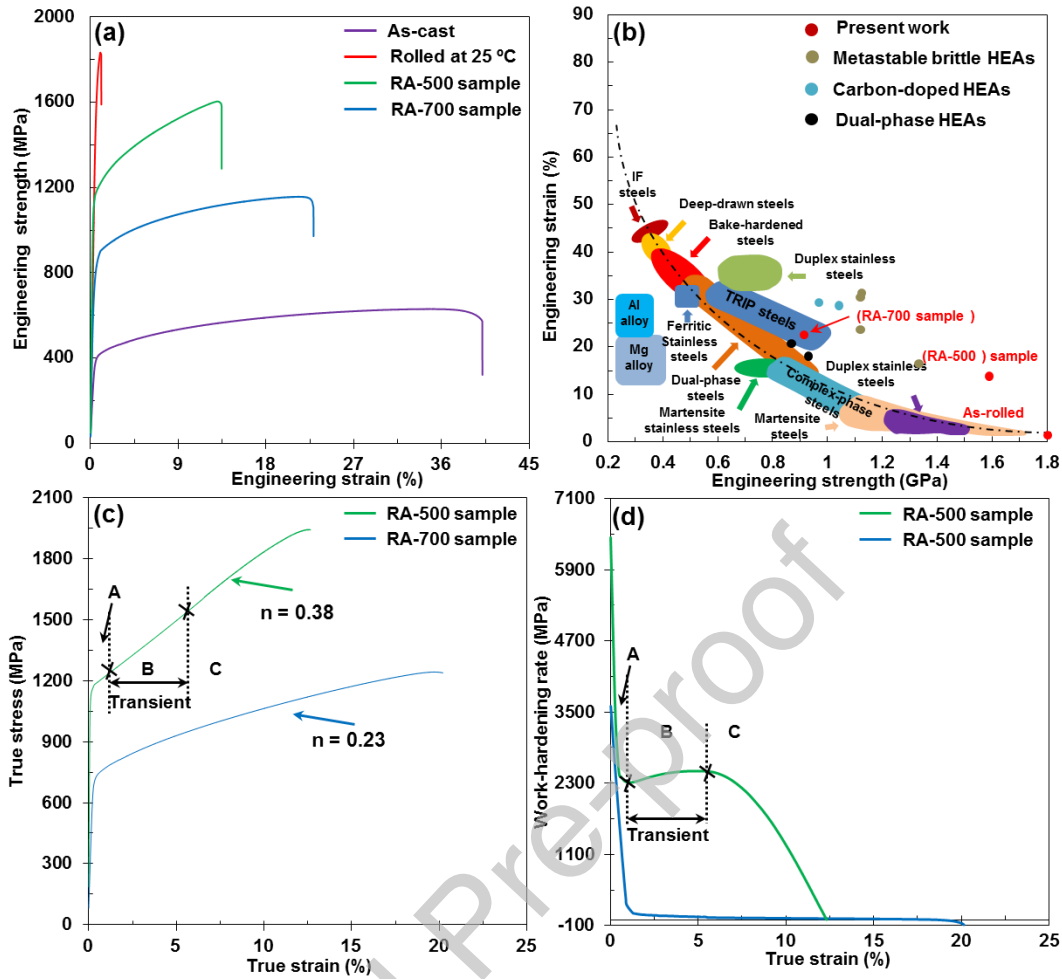RA-500 sample. (g_1–g_5) The corresponding STEM-EDS maps of γ' precipitates in the RA-700 sample.

Fig. 2. (a) Engineering tensile stress–strain curves of the $(CoCrNi)_{94}Ti_3Al_3$ alloy with different processing treatments at room temperature. (b) Comparison of the tensile properties between the $(CoCrNi)_{94}Ti_3Al_3$ alloy and other engineering materials [34–37]. (c) True stress–strain curves and (d) work-hardening response of the $(CoCrNi)_{94}Ti_3Al_3$ alloy after RA-500 and RA-700 treatments, respectively.

Table 2 Yield strength (YS), ultimate tensile strength (UTS), fracture strain (FS), and Vickers hardness determined in the $(CoCrNi)_{94}Ti_3Al_3$ alloys with different treatments.

Treatment	YS (GPa)	UTS (GPa)	FS (%)	Hardness (Hv)
As-cast	0.41	0.63	40.2	298.5
Rolled at 25 °C	1.63	1.83	1.1	540.3
RA-500	1.20	1.60	13.5	525.3

RA-700	0.90	1.15	22.9	435.4

The engineering tensile stress–strain curves of the $(CoCrNi)_{94}Ti_3Al_3$ alloy with different treatments are shown in Fig. 2(a), and the featured data for tensile and hardness are listed in Table 2. For the as-cast samples, the yield strength (YS) was 0.41 GPa, the ultimate tensile strength (UTS) was 0.63 GPa, and the fracture strain was 40.2%. After cold rolling with a 70% thickness reduction at 25 °C, the YS and UTS increased to 1.63 GPa and 1.83 GPa, respectively, but the fracture strain sharply decreased to only 1.1%. The YS, UTS, and fracture strain were 0.90 GPa, 1.15 GPa, and 22.9% after RA-700 treatment. After annealing at the optimal condition of RA-500, the YS, UTS, and fracture strain of the alloy retained 1.20 GPa, 1.60 GPa, and 13.5%, respectively. Apparently, an excellent combination of strength and ductility has been achieved. Fig. 2(b) demonstrates a comparison of tensile properties (i.e., engineering strength and engineering strain) between the $(CoCrNi)_{94}Ti_3Al_3$ alloy in the present study and other engineering materials [34–37]. The alloy with RA-500 treatment exhibited a better combination of strength and ductility. Moreover, the true stress–strain curves of RA-500/700 samples are also shown in Fig. 2(c). The true stress–strain curve of the RA-500 sample shows a typical transient hardening at strains ranging from 1.0% to 5.4%, typical of strain hardening response. Meanwhile, the comparison of the strain hardening exponent (n) between the $(CoCrNi)_{94}Ti_3Al_3$ alloys fabricated in this study and other engineering alloys is shown in Table 3. Apparently, the RA-500 sample exhibited a higher strain hardening exponent. Normally, a higher n value represents a stronger strain hardening effect and better formability, which suggests that the material can be greatly strain-hardened during plastic deformation.

11

Table 3 Comparison of the strain hardening exponent (n) between the present $(CoCrNi)_{94}Ti_3Al_3$ alloy and other reported engineering alloys.

Alloys	strain hardening exponent (n)
$(CoCrNi)_{94}Ti_3Al_3$ alloy (RA-500)	0.38
$(CoCrNi)_{94}Ti_3Al_3$ alloy (RA-700)	0.23
316L stainless steel	0.39 [38]
Al alloys sheet	< 0.33 [39]
Pure Cu	0.35 [40]
CrMnFeCoNi	0.16/0.32 [41]
TWIP $Cr_{26}Mn_{20}Fe_{20}Co_{20}Ni_{14}$	0.23 [42]
$Fe_{35}Ni_{35}Cr_{20}Mn_{10}$	0.24/0.29 [43]
FeMnNi	0.38/0.17/0.15 [44]

Furthermore, Fig. 2(d) presents the work-hardening behavior of RA-500/700 samples as a function of the true strain. The RA-700 sample only shows a monotonic two-stage decrease in the work-hardening rate. By contrast, a three-stage work-hardening behavior following yielding was observed in the RA-500 sample. The initial rapid drop of work hardening rates corresponding to stage A (0.0% to 1.0%) indicates the start of plastic deformation after yielding, which is normally observed in fcc-based alloys [35]. Upon straining to stage B (1.0% to 5.4%), the work hardening rate increases notably for 2.5 GPa at 5.4% strain. This double-yielding behavior is similar to the TRIP/TWIP effect [45, 46]. In stage C (5.4% to 12.6%), the work hardening rate decreases gradually again.
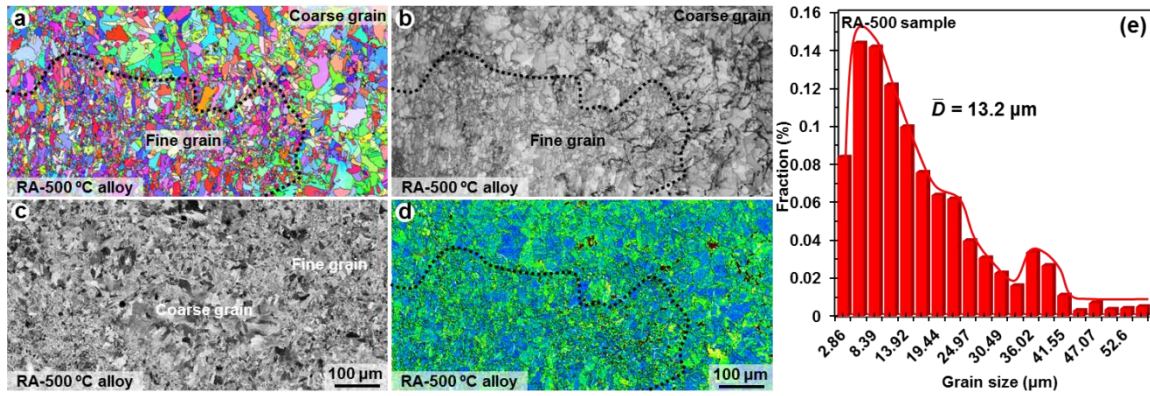
Fig. 3. (a) IPF, (b) IQ map, and (c) SEM image showing grain structure of the $(CoCrNi)_{94}Al_3Ti_3$ alloy with RA-500 treatment after tensile testing. (d) KAM map of the $(CoCrNi)_{94}Al_3Ti_3$ alloy with RA-500 treatment. (e) Grain size distribution of the $(CoCrNi)_{94}Al_3Ti_3$ alloy with RA-500 treatment.

Inverse Pole Figure (IPF), Image Quality (IQ) map, and SEM image of the $(CoCrNi)_{94}Ti_3Al_3$ alloy (tip of the tensile specimen after tensile testing) after RA-500 treatment are shown in Fig. 3(a–c), and the corresponding grain size distribution is shown in Fig. 3(e). The obvious existence of refined heterogeneous grain structure with an average grain size of ~ 13.2 μm was detected. The resultant heterogeneous grain structure contained two types of grains with different length scales and sizes: the coarsening grains (> 11 μm) constituted an area fraction of ~ 49.2%, and the relative fine grains (< 11 μm) comprised an area fraction of ~ 50.8%. Therefore, we successfully obtained a multi-scale heterogeneous structure with matrix and precipitate through single-step cold rolling and annealing in the RA-500 sample. Additionally, the relatively homogeneous matrix with an average grain size of ~ 25.7 μm was observed in the IPF (Fig. 4(a)), IQ map (Fig. 4(b)), and SEM image (Fig. 4(c)) of the RA-700 sample. Moreover, the IQ+GOS (grain orientation spread) map in Fig. 4(d) indicated that the resultant homogeneous grain structure contained the mixture of the partial-recrystallization grains (PR grains) constituted a volume fraction of ~ 17.74%, the

13

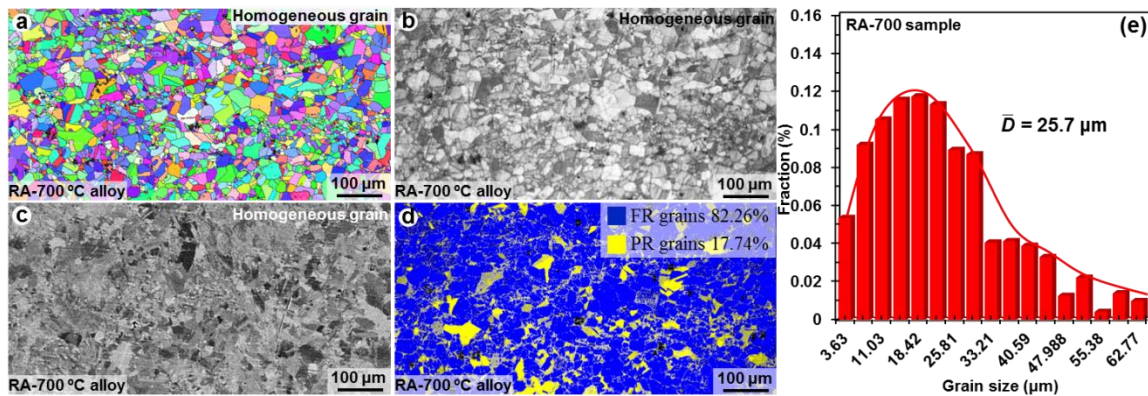fully-recrystallization grains (FR grains) comprised a volume fraction of ~ 82.26%.

Fig. 4. (a) IPF, (b) IQ maps, and (c) SEM image showing grain structure of the $(CoCrNi)_{94}Al_3Ti_3$ alloy with RA-700 treatment after tensile testing. (d) IQ+GOS map showing the volume fraction of fully-crystallization grains (FR) and partial-recrystallization grains (PR). (e) Grain size distribution of the $(CoCrNi)_{94}Al_3Ti_3$ alloy with RA-700 treatment.

It is clear in Fig. 2(a) that the one-step rolling with annealing treatment significantly increased the strength of the as-cast $(CoCrNi)_{94}Ti_3Al_3$ alloy. The rolling/annealing-induced variation in mechanical properties depends closely on the heterogeneous matrix grains and γ' precipitates (refer to the microstructure characteristics). The pronounced strengthening and the exceptional work-hardening ability in hetero-structured materials are reported to be attributed to the efficient strain hardening rate [20–23, 47, 48]. This mechanism can be explained as follows: Firstly, both coarsening and fine grains deform in an elastically similar manner to their homogeneous coarsening grains counterparts [49]. With increasing the true stain, the fine grains continue deforming elastically while the coarsening grains begin to deform plastically, resulting in a deformation incompatibility and composite-like behavior. Thus, to accommodate the deformation incompatibility near grain boundaries and interfaces

14

separating the coarsening- and fine-grain regions, geometrically necessary dislocations (GNDs) piled up and blocked at grain boundaries of coarsening grains are required. The variations in local misorientation qualitatively reflected the degree of plastic deformation or defect density, and additional stress was introduced into the boundaries of adjacent grains to guarantee strain compatibility during plastic deformation, which increased the density of GND [27, 50]. Correspondingly, the kernel average misorientation (KAM) map of the RA-500 sample is shown in Fig. 3(d). The relatively high local misorientation is obviously seen in the coarsening-grain region. These GNDs may interact with mobile dislocations to increase the density of mobile dislocations in coarsening grains due to dislocation interaction and entanglement. Consequently, stage B of the work hardening rate of the hetero-structured RA-500 sample maintains a near-constant value due to the severe deformation of coarsening grains, and subsequently the deformation of fine grains causes a gradual decrease in the work-hardening rate. Essentially, the enhanced strain hardening rate and work-hardening rate induced by heterogeneous matrix grains (i.e., soft coarse grains and fine hard grains) are similar to the TRIP effect (the occurrence of stress and strain hardening induced by hard fresh martensite and soft austenite [51–54]) and TWIP effect (changing the dislocation accumulation rate and hardening the slip system directly through the Hall–Petch effect [55, 56]). For instance, the dislocation hardening of the stable fcc phase and increased ductility induced by transformation-induced hardening of the metastable hexagonal closed-packed (hcp) phase are widely researched in the FeMnCrCo-systems MEAs [53, 54]. Meanwhile, the $Fe_{40}Mn_{40}Cr_{10}Co_{10}$ MEA exhibited an enhanced strain hardening rate and tensile strength due to the strong twin–twin and twin–slip interactions where twin boundaries reduce the mean

free path of dislocations [56]. Finally, a three-stage work-hardening behavior was present following yield, as shown in Fig. 2(d). Additionally, the hetero-structured RA-500 sample showed a much higher work-hardening rate in comparison with its homogenous RA-700 sample, which indicates that the mechanical incompatibility induced by heterogeneous matrix grains and γ' precipitates plays a crucial role in the increment in work-hardening rate further.
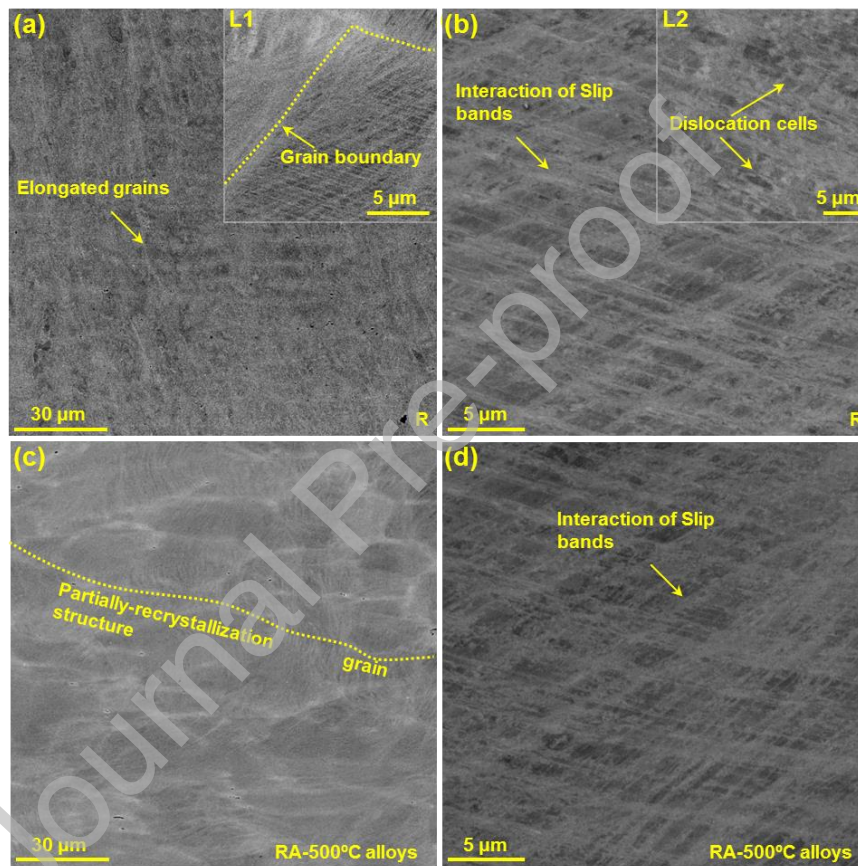
Fig. 5. ECCI microstructural analysis of the $(CrCoNi)_{94}Al_3Ti_3$ alloys under different conditions, i.e. (a) and (b) Rolling, (c) and (d) RA-500 treatment.

Different from the single heterogeneous matrix in the pure CoCrNi alloy reported in previous studies [20–23], the refined heterogeneous γ' precipitates detected in this study also played an important role in tuning the trade-off of strength and ductility. On the one hand, a high volume fraction of small precipitates is preferred to generate effective precipitation

16

strengthening according to the Orowan strengthening theory [57]. Compared with the alloy with RA-700 treatment, the high strength observed in the sample after RA-500 treatment is partially attributed to the high number density of fine γ' precipitates, the corresponding strengthening contribution of γ' precipitates will be calculated in the following sections. On the other hand, the previous studies have indicated that the heterogeneity in γ' precipitates delivered the difference in precipitation hardening effect and also promoted strain partitioning further [22, 58]. Meanwhile, the ultrafine γ' precipitates have a coherent orientation relationship with their surrounding fcc matrix, as shown in Fig. 1(c). The associated elastic interaction between γ' precipitates and dislocations is hence lowered. This can prevent crack initiation at the precipitate-matrix interfaces owing to negligible strain accumulation and maintaining the uniform plastic deformation [59].

Furthermore, the other positive effects of strain hardening capacity might be attributed to the formation of various kinds of heterogeneous ultra-fine crystalline defects. The ECCI microstructural analysis of the as-rolled samples without and with RA-500 treatment after tensile testing in Fig. 5 indicated that many slip bands (~ 0.8 μm) occur within the grain matrix and interact with each other. Slip bands, which are formed as a result of the planar slip and occur in MEAs/HEAs along with lattice friction stress, have been recognized to accommodate plastic deformation [35, 60, 61]. Moreover, the detailed microstructural evolution of the $(CoCrNi)_{94}Al_3Ti_3$ alloy after tensile testing is shown in Fig. 6. BF-TEM images in Fig. 6(a, b) indicated that the typically elongated grain microstructure is detected in the as-rolled alloy with high-density dislocations inside. Abundant immobile LC Locks accompanied with SFs are also detected in the matrix, as shown in Fig. 6(c). These

crystalline defects of different sizes, such as SFs and LC Locks on multiple {111} planes (~ 2 nm), and deformation twins (DTs, 5–10 nm), are also observed in the RA-500 sample, as shown in the TEM image of Fig. 6(e–g). DTs, acting as the additional plasticity mode, are the key microstructural origin for the remarkably enhanced strength/ductility and superior strain hardening capacity. Generally, apart from acting as the plastic carrier, DTs could induce grain refinement effect by introducing extra interfaces and thereby notably reduce the dislocation mean free path, leading to a pronounced dynamic Hall–Petch effect [61, 62]. Moreover, in addition to endowing slippery pathways to facilitate the glide of dislocations for plasticity [63], these extra twin boundaries could also provide effective obstacles against dislocation motion, and their subsequent interplays can increase the capacity of dislocation gathering [64, 65]. Additionally, SFs are widely found at both room and cryogenic temperatures and are believed to be the dominant deformation modes of γ'-hardened HEAs/MEAs [12, 66]. Although the hardening effects of SFs may not be as effective as DTs [67], the high number density of SFs can still benefit the strain hardening by acting as the barrier to impede the propagation of dislocations [12]. Moreover, like the SFs, dislocations from four directions can be pinned by the LC locks, and other dislocations are also difficult to move near the LC locks, then resulting in dislocation pile-up [68], which also plays a positive role in the strengthening and strain hardening of HEAs/MEAs [3, 69–71]. When further increasing the annealing temperatures to 700 °C, the BF-TEM images in Fig. 6(h, i) show that the alloy contained recrystallized grains in which an interaction between dislocations with twins occurred.
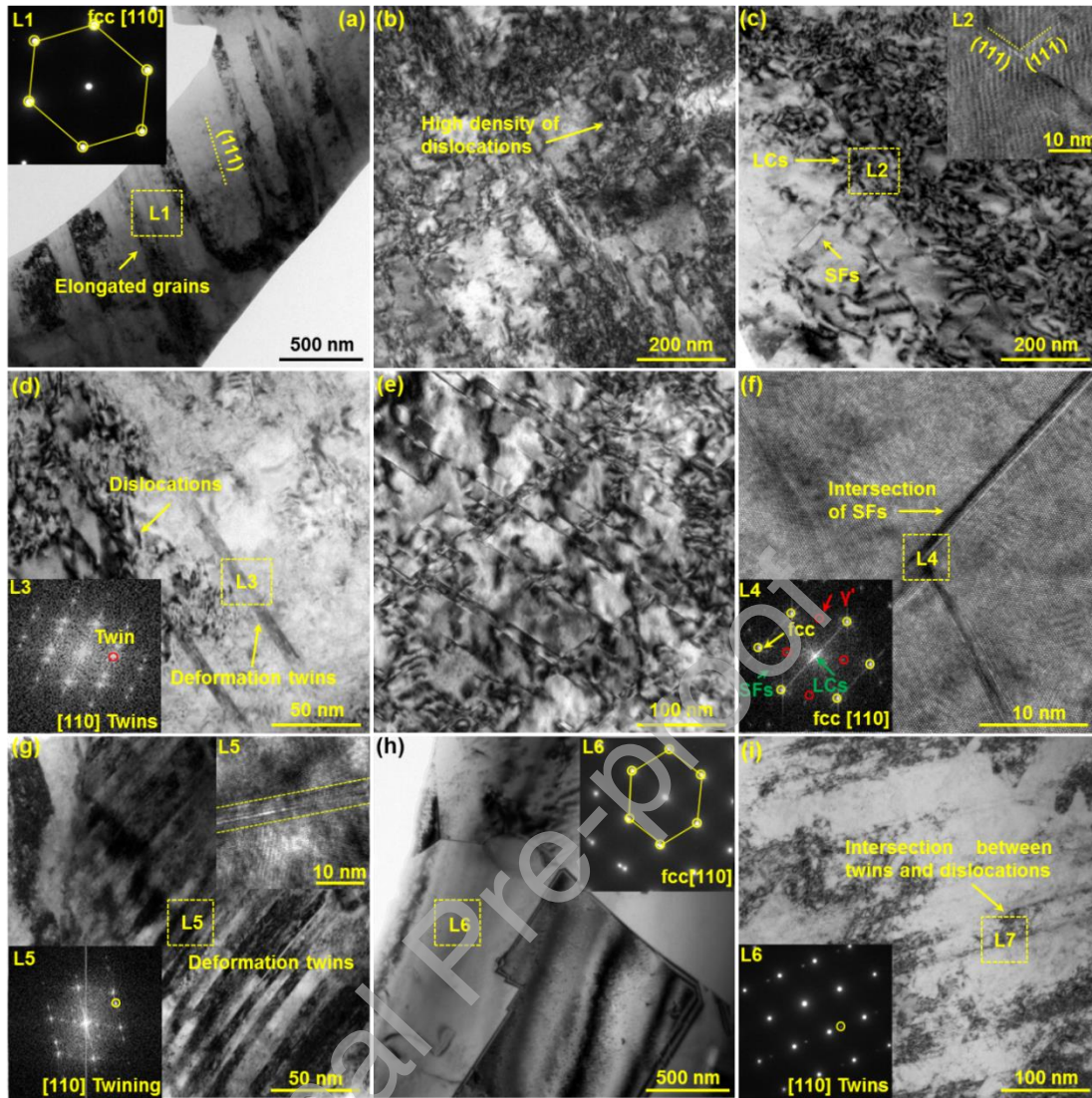
Fig. 6. (a)–(d) Detailed microstructural analysis of the as-rolled (CoCrNi)$_{94}$Al$_3$Ti$_3$ alloy: (a) the elongated grains and SAED pattern L1, showing the fcc matrix with a (111) local rolling texture; (b) BF-TEM image showing the high density of dislocations; (c) BF-TEM image and SAED pattern L2, showing the formation of SFs and LCs; (d) BF-TEM image and SAED pattern L3, showing the formation of deformation twins. (e)–(g) Detailed microstructural analysis of the (CoCrNi)$_{94}$Al$_3$Ti$_3$ alloy treated by RA-500 treatment: (e) and (f) BF-TEM image and HR-TEM image and FTT patterns L4, showing the γ' precipitates, SFs and LCs; (g) BF-TEM image and SAED pattern L5 indicating the formation of nanotwins. (h) and (i) Detailed microstructural analysis of the (CoCrNi)$_{94}$Al$_3$Ti$_3$ alloy treated by RA-700 treatment: (h) BF-TEM image showing the fully-recrystallized structures; (i) BF-TEM image implying the interaction between

19

deformation twins with certain dislocations.

As demonstrated in Figs. 5 and 6, the $(CoCrNi)_{94}Al_3Ti_3$ alloy after RA-500 treatment showed abundant deformation modes, which are different from that of the reported γ'-hardened HEAs/MEAs [12, 66]. In the present study, apart from SFs, LC Locks, deformation twins, and slip bands occurred during the tensile deformation of RA-500 sample. Based on a three-stage work-hardening behavior, we believe that the localized strains in the coarse grains result from the high stress and thus stimulate the formation of deformation twins. These additional slip bands and deformation twins are beneficial to the strain hardenability and ductility of the alloy.

Also, from the above microstructural observations, for the $(CrCoNi)_{94}Al_3Ti_3$ alloy, potential strengthening mechanisms should involve the combination of grain boundary strengthening (σ_g), dislocation strengthening (σ_{dis}), and precipitation strengthening (σ_p), in addition to its lattice friction strength σ_0. For simplicity, the contribution of main mechanisms responsible for the strengthening of the RA-500 sample can be expressed as Eq. (1).

$$\sigma_y = \sigma_0 + \sigma_g + \sigma_{dis} + \sigma_p \tag{1}$$

where σ_0 is a constant (218 MPa for CoCrNi alloy [15]).

3.1. Grain refinement strengthening

EBSD results show the obvious decrease in the average grain size of the fcc matrix after RA-500 treatment, as shown in Fig. 3(a). The part of strengthening effects by grain refinement (σ_g) can be calculated via the Hall–Petch relationship as follows [72]:

$$\sigma_g = K \cdot d^{-0.5} \tag{2}$$

where K is a constant (265 MPa mm$^{1/2}$ for CoCrNi MEA [15]) and d is the average grain size of the $(CrCoNi)_{94}Al_3Ti_3$ alloy under RA-500 condition (~ 13.2 μm). As a consequence, the strength contribution from grain refinement to yield strength is evaluated as ~ 72.9 MPa.

3.2. Dislocation strengthening

The contribution of σ_{dis} can be estimated according to Taylor's hardening law [73]:

$$\sigma_{dis} = M \cdot \alpha \cdot G \cdot b \cdot \rho^{0.5} \tag{3}$$

where M, α, G, b, and ρ are the Taylor factor, empirical constant, shear modulus, Burgers vector, and dislocation density, respectively. For the CoCrNi alloy, the above parameters are $M = 3.06$ [74], $\alpha = 0.2$ [75], $G = 85$ GPa [76], $b = 0.253$ nm [12]. Usually, the total dislocation density is composed of GND and statistical storage dislocation (SSD). GND is caused by uniform deformation. It is mainly distributed in the grain boundary region and the restricted boundary region, while the SSD is mainly distributed inside the grain, so the main contribution of dislocation enhancement comes from the GND. According to Eq. (4) proposed by Zaiser et al. [77], the KAM map can be used to calculate GND by combining local strain.

$$\rho_{GND} = 2 \cdot \vartheta / (\mu \cdot b) \tag{4}$$

where ϑ is the average value of KAM (0.938), μ is the step size during EBSD measurement. Therefore, the strength contribution from dislocation strengthening to yield strength is evaluated as ~ 566.1 MPa.

3.3. Precipitation strengthening

The fine γ' precipitates have the size distribution of a dominant number of particles less than 100 nm (Fig. 1(a)). During deformation, γ' precipitates act as hard phases at grain boundaries and in the fcc matrix, which interact with dislocations through the pining effect and block the dislocation movement further (Orowan-type). Correspondingly, the precipitation strengthening can be calculated by Orowan–Ashby equation [78]:

$$\sigma_{\text{dis}} = 0.13 \cdot G \cdot b/\lambda \cdot \ln\frac{D}{2b} \qquad (5)$$

$$\lambda = D \cdot [(2 \cdot V_p)^{-1/3} - 1] \qquad (6)$$

where G and b represent the shear modulus and Burgers vector of CoCrNi alloy, while D, λ, and V_p represent the average diameter, average inter-particulate spacing, and volume fraction of γ' precipitates, respectively. Thus, the strength contribution from precipitation strengthening to yield strength is estimated as ~ 403.4 MPa.

Correspondingly, the strengthening contributions from grain boundary strengthening, dislocation strengthening, and precipitation strengthening are calculated to be ~ 72.9 MPa, ~ 566.1 MPa, and ~ 403.4 MPa, respectively, the total yield strength estimated by Eq. (1) would be 1.26 GPa, which is approaching to the measured yield strength of 1.28 GPa.
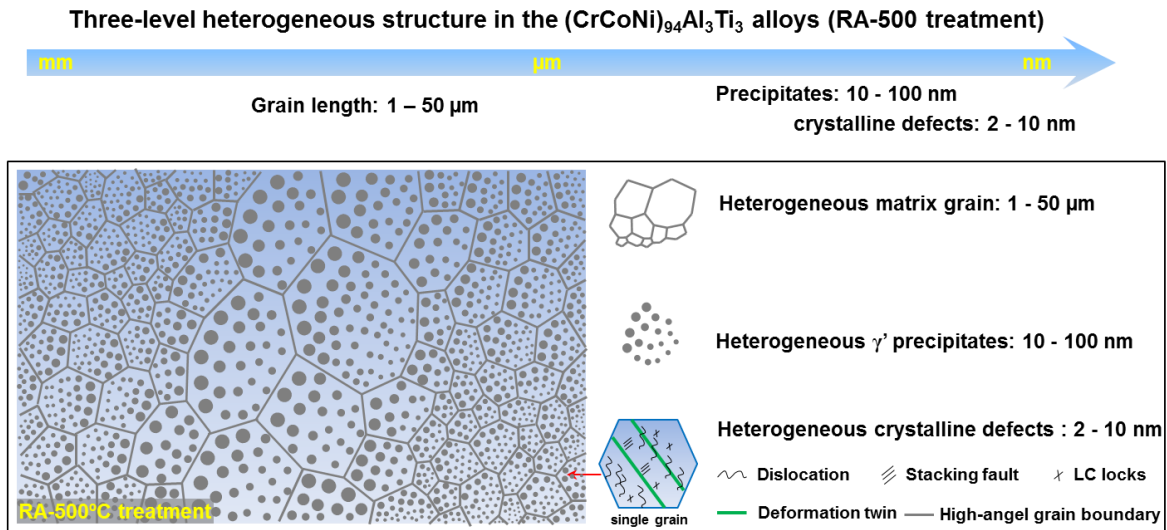
Three-level heterogeneous structure in the $(CrCoNi)_{94}Al_3Ti_3$ alloys (RA-500 treatment)

mm   μm   nm

Grain length: 1 – 50 μm   Precipitates: 10 - 100 nm
crystalline defects: 2 - 10 nm

Heterogeneous matrix grain: 1 - 50 μm

Heterogeneous γ' precipitates: 10 - 100 nm

Heterogeneous crystalline defects : 2 - 10 nm

∿ Dislocation   ∥ Stacking fault   ⅄ LC locks

— Deformation twin   — High-angel grain boundary

single grain

RA-500°C treatment

Fig. 7. Schematic illustration showing the microstructural evolution during different processing routes in the present work.

A representative diagram showing the microstructural characteristics in the studied $(CoCrNi)_{94}Al_3Ti_3$ alloy after RA-500 treatment is schematically illustrated in Fig. 7. The multi-scale heterogeneous structures could be architected by a single rolling and annealing treatment. The enhanced mechanical properties (UTS of 1.60 GPa and fracture strain of 13.5%) mainly originate from three aspects: (i) the refined heterogeneous matrix grains (1–50 μm) brought grain boundary strengthening and exceptional work-hardening ability; (ii) the ultrafine heterogeneous γ' precipitates (10–100 nm) delivered effective precipitation strengthening; (iii) it is probable that the strengthening and hardening also originated from the capability of various crystalline defects with different sizes (i.e., the SFs, LCs, DTs, and slip bands) to accommodate dislocations, which benefited the strain hardenability of the alloy and thus led to good ductility.

4. Conclusions

In this work, we explored a feasible single-step heat treatment to develop a $(CoCrNi)Ti_3Al_3$

alloy with multi-scale heterogeneous structures, which resulted in the simultaneous improvement of strength and ductility. The major conclusions were made as follows.

(1) The $(CoCrNi)Ti_3Al_3$ alloy with an excellent strength–ductility synergy was achieved through single-step rolling and annealing. A good combination of yield strength of 1.47 GPa, UTS of 1.60 GPa, and fracture strain of 13.1% has been obtained after RA-500 treatment.

(2) The alloy exhibited multi-scale heterogeneous structures that contains the favorable heterogeneous fcc matrix grains (1–40 μm) and the coherent spherical γ' nanoprecipitates (10–100 nm), together with the high number density of 2–10 nm crystalline defects (i.e. dislocations, small stacking faults, Lomer–Cottrell locks, and ultrafine nanotwins).

(3) This investigation provides an economical and efficient way to fabricate high strength and ductile CoCrNi-based MEAs. Meanwhile, it promotes to unravel the deformation mechanisms of MEAs with characteristic microstructures.

Acknowledgments

References

[1] J.W. Yeh, S.K. Chen, S.J. Lin, J.Y. Gan, T.S. Chin, T.T. Shun, C.H. Tsau, S.Y. Chang, Adv. Eng. Mater. 6 (2004) 299–303.

[2] B. Cantor, I.T.H. Chang, P. Knight, A.J.B. Vincent, Mater. Sci. Eng. A 375–377 (2004) 213–218.

[3] H. Huang, J.Y. Wang, H.L. Yang, S. Ji, H.L. Yu, Z.L. Liu, Scr. Mater. 188 (2020) 216–221.

[4] B. Gludovatz, A. Hohenwarter, K.V.S. Thurston, H.B. Bei, Z.G. Wu, E.P. George, R.O. Ritchie, Nat. Commun. 7 (2016) 10602–10609.

[5] Z. Zhang, H. Sheng, Z. Wang, B. Gludovatz, Z. Zhang, E.P. George, Q. Yu, S.X. Mao, R.O. Ritchie, Nat. Commun. 8 (2017) 14390.

[6] G. Laplanche, A. Kostka, C. Reinhart, J. Hunfeld, G. Eggeler, E.P. George, Acta Mater. 128 (2017) 292–303.

[7] J.S. Miao, C. Slone, S. Dasari, M. Ghazisaeidi, R. Banerjee, E.P. George, M.J. Mills, Acta Mater. 210 (2021) 116829.

[8] J.Y. Wang, H.L. Yang, J.M. Ruan, Y. Wang, S.X. Ji, J. Mater. Res. 34 (2019) 2126–2136.

[9] I. Moravick, L. Gouvea, J. Cupera, I. Dlouhy, J. Alloy. Compd. 5 (2018) 979–988.

[10] Y.J. Shi, Y.D. Wang, S.L. Li, R.G. Li, Y.K. Wang, Mater. Sci. Eng. A 788 (2020) 139600.

[11] H. Feng, H.B. Li, X.L. Wu, Z.H. Jiang, S. Zhao, T. Zhang, D. Xu, S. Zhang, H.C. Zhu, B.B. Zhang, M.X. Yang, J. Mater. Sci. Technol. 34 (2018) 1781–1790.

[12] Y.L. Zhao, T. Yang, Y. Tong, J. Wang, J.H. Luan, Z.B. Jiao, D. Chen, Y. Yang, A. Hu, C.T. Liu, J.J. Kai, Acta Mater. 138 (2017) 72–82.

[13] R.B. Chang, W. Fang, H.Y. Yu, X. Bai, X. Zhang, B.X. Liu, F.X. Yin, Scr. Mater. 172 (2019) 144–148.

[14] J.Y. Wang, J.P. Zou, H.L. Yang, Z.L. Liu, S.X. Ji, Mater. Sci. Eng. A 843 (2022) 143129.

[15] S. Yoshida, T. Bhattacharjee, Y. Bai, N. Tsuji, Scr. Mater. 134 (2017) 33–36.

[16] K. Jiang, B. Gan, J.G. Li, Q.B. Dou, T. Suo, Mater. Sci. Eng. A 816 (2021) 141298.

[17] H. Shahmir, J.Y. He, Z.P. Lu, M. Kawasaki, T.G. Langdon, Mater. Sci. Eng. A 676 (2016) 294–303.

[18] S.J. Sun, Y.Z. Tian, H.R. Lin, X.G. Dong, Y.H. Wang, Z.J. Zhang, Z.F. Zhang, Mater. Des. 133 (2017) 122–127.

[19] K. Lu, Science 345 (2014) 1455–1456.

[20] X.L. Wu, P. Jiang, L. Chen, J.F. Zhang, F.P. Yuan, Y.T. Zhu, Mater. Res. Lett. 2 (2014) 185–191.

[21] C.E. Slone, J. Miao, E.P. George, M.J. Mills, Acta Mater. 165 (2019) 496–507.

[22] M.X. Yang, D.S. Yan, F.P. Yuan, P. Jiang, E. Ma, X.L. Wu, Proc. Natl. Acad. Sci. U. S. A. 115 (2018) 7224–7229.

[23] X.H. Du, W.P. Li, H.T. Chang, T. Yang, G.S. Duan, B.L. Wu, J.C. Huang, F.R. Chen, C.T. Liu, W.S. Chuang, Y. Lu, M.L. Sui, E.W. Huang, Nat. Commun. 11 (2020) 2390.

[24] J.Y. Wang, J.P. Zou, H.L. Yang, L.J. Zhang, Z.L. Liu, X.X. Dong, S.X. Ji, J. Mater. Sci. Technol. 127 (2022) 61–70.

[25] X. Wu, M. Yang, F. Yuan, G. Wu, Y. Wei, X. Huang, Y. Zhu, Proc. Natl. Acad. Sci. U. S. A. 112 (2015) 14501–14505.

[26] L.H. Qian, K.F. Li, F. Huang, D.D. Li, T.L. Wang, J.Y. Meng, F.C. Zhang, Scr. Mater. 183 (2020) 96–101.

[27] C.X. Huang, Y.F. Wang, X.L. Ma, S. Yin, H.W. Höppel, M. Göken, X.L. Wu, H.J. Gao, Y.T. Zhu, Mater. Today 21 (2018) 713–719.

[28] X.L. Ma, C.X. Huang, J. Moering, M. Ruppert, H.W. HÖppel, M. GÖken, J. Narayan, Y. Zhu, Acta Mater. 116 (2016) 43–52.

[29] Q.S. Pan, L.X. Zhang, R. Feng, Q.H. Lu, L. Lu, Science 374 (2021) 984–989.

[30] Z. Cheng, H.F. Zhou, Q.H. Lu, H.J. Gao, L. Lu, Science 362 (2018) 559–566.

[31] H.Z. Zhao, Z.S. You, N.R. Tao, L. Lu, Acta Mater. 210 (2121) 116830.

[32] X. Bai, W. Fang, J.W. Lv, R.B. Chang, H.Y. Yu, J.H. Yan, X. Zhang, Intermetallics 132 (2021) 107125.

[33] N. An, Y.N. Sun, Y.D. Wu, J.J. Tian, Z.R. Li, Q. Li, J.Y. Chen, X.D. Hui, Mater. Sci. Eng. A 798 (2020) 140213.

[34] J.Y. He, H. Wang, H.L. Huang, X.D. Xu, M.W. Chen, Y. Wu, X.J. Liu, T.G. Nieh, K. An, Z.P. Lu, Acta Mater. 2016 (102) 187–196.

[35] H.L. Huang, Y. Wu, J.Y. He, H. Wang, X.J. Liu, K. An, W. Wu, Z.P. Lu, Adv. Mater. 29 (2017) 1701678.

[36] Z.W. Wang, I. Baker, W. Guo, J.D. Poplawsky, Acta Mater. 126 (2017) 346–360.

[37] I. Baker, F.L. Meng, M. Wu, A. Brandenberg, J. Alloy. Compd. 656 (2016) 458–464.

[38] X.H. Chen, J. Lu, L. Lu, K. Lu, Scr. Mater. 52 (2005) 1039–1044.

[39] S. Tsuchida, H. Yokoi, N. Kanetake, J. Jpn. Inst. Met. 4 (2009) 195–200.

[40] A. Misra, X. Zhang, D. Hammon, R.G. Hoagland, Acta Mater. 53 (2005) 221–226.

[41] Z.L. Yang, M.X. Yang, Y. Ma, L.L. Zhou, W.Q. Cheng, F.P. Yuan, X.L. Wu, Mater. Sci. Eng. A 19 (2020) 139854.

[42] X.Z. Gao, Y.P. Lu, J.Z. Liu, J. Wang, T.M. Wang, Y.H. Zhao, Materialia 8 (2019) 100485.

[43] J. Zhou, H.C. Liao, H. Chen, A.J. Huang, Mater. Charact. 178 (2021) 111251.

[44] S.R. Jha, K. Biswas, N.P. Gurao, Mater. Sci. Eng. A 826 (2021) 141965.

[45] M. Marteleur, F. Sun, T. Gloriant, P. Vermaut, P.J. Jacques, F. Prima, Scr. Mater. 66 (2012) 749–752.

[46] K. Yao, X.H. Min, Acta Mater. 226 (2022) 117641.

[47] X. Zhang, P. Wang, D.Z. Li, Y.Y. Li, J. Mater. Sci. Technol. 72 (2021) 180–188.

[48] G. Niu, H.S. Zurob, R.D.K. Misra, H.B. Wu, Y. Zou, J. Mater. Sci. Technol. 20 (2022) 133–138.

[49] X.L. Wu, Y.T. Zhu, Mater. Res. Lett. 5 (2017) 527–532.

[50] S.C. Li, C.Y. Guo, L.L. Hao, Y.L. Kang, Y.G. An, Mater. Sci. Eng. A 759 (2019) 624–632.

[51] X.L. Wu, M.Y. Yang, F.P. Yuan, L. Chen, Y.T. Zhu, Acta Mater. 112 (2016) 337–346.

[52] R. Wei, K.S. Zhang, L.B. Chen, Z.H. Han, T. Wang, C. Chen, J.Z. Jiang, T.W. Hu, F.S. Li, J. Mater. Sci. Technol. 57 (2020) 153–158.

[53] Z.M. Li, K.G. Pradeep, Y. Deng, D. Raabe, C.C. Tasan, Nature 534 (2016) 227–230.

[54] P.J. Zhang, S.H. Wang, Y.K. Lv, L.S. Chen, K. Liu, D.G. Zhao, J. Mater. Res. Technol. 15 (2021) 2145–2151.

[55] A. Nabizada, A. Zarei-Hanzaki, H.R. Abedi, M.H. Barati, P. Asghari-Rad, H.S. Kim, Mater. Sci. Eng. A 802 (2021) 140600.

[56] S. Picak, J. Liu, C. Hayrettin, W. Nasim, D. Canadinc, K. Xie, Y.I. Chumlyakov, I.V. Kireeva, I. Karaman, Acta Mater. 181 (2019) 555–569.

[57] Z.F. Hao, G.L. Xie, X.H. Liu, Q. Tan, R. Wang, J. Mater. Sci. Technol. 98 (2022) 1–13.

[58] F. He, Z.S. Yang, S.F. Liu, D. Chen, W.T. Lin, T. Yang, D.X. Wei, Z.J. Wang, J.C. Wang, J.J. Kai, Int. J. Plast. 144 (2021) 103022.

[59] S.H. Jiang, H. Wang, Y. Wu, X.J. Liu, H.H. Chen, M.J. Yao, B. Gault, D. Ponge, D. Raabe, A. Hirata, M.W. Chen, Y.D. Wang, Z.P. Lu, Nature 544 (2017) 460–464.

[60] Z.W. Wang, I. Baker, Z.H. Cai, S. Chen, J.D. Poplawsky, W. Guo, Acta Mater. 120 (2016) 228–239.

[61] F. Otto, A. Dlouhý, C. Somsen, H. Bei, G. Eggeler, E.P. George, Acta Mater. 61 (2013) 5743–5755.

[62] M. Schneider, G. Laplanche, Acta Mater. 204 (2021) 116470.

[63] Q. Ding, X. Fu, D. Chen, H. Bei, B. Gludovatz, J. Li, Z. Zhang, E.P. George, Q. Yu, T. Zhu, R.O. Ritchie, Mater. Today 25 (2019) 21–27.

[64] K. Lu, L. Lu, S. Suresh, Science 324 (2009) 349–352.

[65] L. Lu, Z.S. You, K. Lu, Scr. Mater. 66 (2012) 837–842.

[66] Y. Tong, D. Chen, B. Han, J. Wang, R. Feng, T. Yang, C. Zhao, Y.L. Zhao, W. Guo, Y. Shimizu, C.T. Liu, P.K. Liaw, K. Inouc, Y. Nagai, J.J. Kai, Acta Mater. 165 (2019) 228–240.

[67] Y. Ma, F.P. Yuan, M.X. Yang, P. Jiang, E. Ma, X.L. Wu, Acta Mater. 148 (2018) 407–418.

[68] L. Dupuy, M.C. Fivel, Acta Mater. 50 (2002) 4873–4885.

[69] J.Y. Wang, H.L. Yang, H. Huang, J.P. Zou, S.X. Ji, Z.L. Liu, Mater. Sci. Eng. A 796 (2020) 139974.

[70] L. Zhang, Z.H. Hu, L. Zhang, H. Wang, J.B. Li, Z. Li, J.X. Yu, B.L. Wu, Scr. Mater. 211 (2022) 114497.

[71] K. Jiang, T.F. Ren, G.B. Shan, T. Ye, L.Y. Chen, C.X. Wang, F. Zhao, J.G. Li, T. Suo,

Mater. Sci. Eng. A 797 (2020) 140125.

[72] N. Hansen, Scr. Mater. 51 (2004) 801–806.

[73] U.F. Kocks, H. Mecking, Prog. Mater. Sci. 48 (2003) 171–273.

[74] T. Zhang, H.G. Li, H. Gong, Y.X. Wu, A.S. Ahmad, X. Chen, J. Alloy. Compd. 884 (2021) 161050.

[75] M.D. Sangid, T. Ezaz, H. Sehitoglu, I.M. Robertson, Acta Mater. 59 (2011) 283–296.

[76] J.Y. Wang, H.L. Yang, H. Huang, J.M. Ruan, S. Ji, J. Alloy. Compd. 798 (2019) 576–586.

[77] M. Zaiser, E.C. Aifantis, Scr. Mater. 48 (2003) 133–139.

[78] F. Chen, Z.N. Chen, F. Mao, T.M. Wang, Z.Q. Cao, Mater. Sci. Eng. A 625 (2015) 357–368.